Article

A Patient-Specific 3D+t Coronary Artery Motion Modeling Method Using a Hierarchical Deformation with Electrocardiogram.

Siyeop Yoon[1,2], Chang Hwan Yoon [3], Eun Ju Chun [4], Deukhee Lee [1,2,*]

1 Center for Medical Robotics, Korea Institute of Science and Technology, 5, Hwarang-ro 14-gil, Seongbuk-gu, Seoul 02792, Korea; h14515@kist.re.kr (S.Y.);
2 Division of Bio-medical Science and Technology, KIST School, Korea University of Science and Technology, Seoul 02792, Korea
3 Cardiovascular Center, Seoul National University Bundang Hospital, Seongnam 13620, Korea; kunson2@snu.ac.kr
4 Department of Radiology, Seoul National University Bundang Hospital, Seongnam, 13620, Korea; humandr@snubh.org
* Correspondence: dkylee@kist.re.kr; Tel.: +82-10-958-5633

Abstract: Cardiovascular-related diseases are one of the leading causes of death worldwide. An understanding of heart movement based on images plays a vital role in assisting the procedure in the postoperative and postoperative processes. In particular, if the shape information can be provided in real-time using the electrocardiogram(ECG) signal using this information, the heart's movement information can be used for cardiovascular analysis and imaging guides during surgery. In this paper, we propose creating a 3D+t cardiac coronary artery model that is rendered in real-time according to the ECG signal. Hierarchical cage-based deformation modeling is used to generate mesh deformation used during the procedure according to the ECG signal. We match the blood vessel's lumen obtained from the ECG-gated 3D+t CT angiography taken at the multiple cardiac phases to derive the optimal deformation. Splines for 3D deformation control points were used to continuously represent the obtained deformation at the multi-view according to the ECG signal. To verify the proposed method, we compared the manually segmented lumen and results of the proposed method for eight patients. The average distance and dice coefficient between the two models was 0.543mm and 0.735, respectively. The required time for registration of the 3D coronary artery model is 23.53 seconds/model. rendering speed to derive the model according to the ECG signal after generating the 3D+t model is faster than 120 FPS.

Keywords: 3D+t modeling; coronary artery; non-rigid registration; cage deformation; 4D CT

1. Introduction

Cardiovascular disease(CVD) is one of the primary causes of death worldwide, with 22.2 million deaths expected by 2030. According to NHANES data from 2013 to 2016, a prevalence of CVD is 48.0% in adults over the age of 20. The prevalence of CVD has a positive correlation between increasing with age [1]. The resulting social cost is estimated to have spent 351.3 billion dollars in the US alone from 2014 to 2015. In particular, cardiovascular disease accounts for 14% of US medical spending, the highest rate among other major diagnostic groups, even compared to cancer more expenditure. This trend is not only similar, but it represents a more significant loss than the report because it has a larger population globally[1].

Providing sufficient information through image analysis acquired in the pre-operative diagnosis stage eliminates unnecessary exams and helps in the patient-specific treatment plans. In particular, since the heart has a motion induced by the heartbeat even in the steady-state of respiratory, image

 doi:10.20944/preprints202009.0085.v1

analysis equipment used in the diagnostic stage acquires spatiotemporal information in the selected heart phase through ECG-gated reconstruction.

The patient-specific 4D heart shape information facilitates the following applications. For example, accurate coronary artery structure acquisition [2,3], analysis of 4D blood flow and stenosis [4–6], removal of motion artifacts in the vascular region[7–9], surgical simulation for each patient [10], postoperative evaluation and analysis [5,6], atrial motion analysis[11,12], vascular motion analysis[13, 14] real-time deformation prediction during surgery combined with 2D images [8].

Especially, cardiac CT angiography (CTA) has an isotropic spatial resolution of less than 0.5 mm, so it can be used to observe the movement of the coronary artery and trabeculae of the ventricle. In addition to grading the degree of calcification of the coronary artery and the total amount of plaque from the CT image, it is also possible to measure the torsion of the coronary artery from a high resolution[15]. This high-resolution spatial information can help the operator perform a procedure appropriate for each patient before and after surgery. However, despite the high spatial resolution of the CTA, the CTA's resolution is 50-200 ms which is lower than the 4D echocardiography (30-100hz) and cardiac MRI(30-50 ms). Therefore, proper shape interpolation to restoring high time resolution information from CTA image is essential to cooperate with the other applications while preserving high-precision anatomical details.

One of the essential requirements of cardiac modeling in many of these applications is that the topology of the mesh model constituting the cardiac model must be consistently preserved. In particular, in the case of a 4D heart model, the mesh should not cause new problems such as self-intersection, and mesh degeneration even if the positions of the vertices constituting the shape change over time. To address these requirements, many researchers employ the template-based registration scheme.

The registration process matches a template model to a target model through geometric shape deformation. The most popular registration algorithm is the iterative closest point(ICP) method that consists of finding the correspondence between two models and finding the optimal transformation[16]. However, the ICP method is sensitive to initial position and noise, and that shape registration is limited up to rigid transformation. Non-rigid registration deals with the deformation of the shape in addition to the rigid transformation. The non-rigid registration is more challenging because non-rigid transformations not only require more correspondence have to be defined, but the solution space is much more extensive[17]. Researches on registration of 3D non-rigid shapes are actively conducted on the methods of delineating shape deformation and shape correspondence.

To describe the deformation of an object to its dynamics and material properties, many researcher assume shape deformation to be a physical model such as a linear elastic model[18], nonlinear elastic model [19,20], viscous fluid [21], and diffusion model [22,23]. In particular, the Large Deformation Diffeomorphic Metric Mapping (LDDMM) framework provides robust deformation as a massive flow consisting of diffeomorphism[24]. However, physical models are computationally expensive and sensitive to mechanical properties. On the other hand, the statistical shape deformation model (SSM) uses a low dimensional statistical model in which shape deformation is inferred from the population[25,26]. Although SSM reduces the computation cost, the shape of variability is limited up to training data. Therefore, the deformation hardly achieves representation of patients' inter-variability, such as topological discontinuity of coronary arteries. Nora et al. described motion modeling problem using the coronary arteries attached to the SSM of muscles [27]. Due to the representation of the coronary artery, the deformation hardly describes the lumen diameter. Instead of modelizing a priori physical and statistical information, there are attempts to estimate the shape transformations with landmarks and coherent motion. Radial basis function is a method of expressing shape deformation as a weighted sum of distance function for control point change[28]. In particular, the thin-plate spline minimizes the bending energy that has a closed-form solution[29]. There is also the most popular form of deformation known as and the B-spline free-form deformation(FFD)[26,30,31], and Rueckert et al. [32] have proved the conditions for FFD to have diffeomorphic deformation. However, this

 doi:10.20944/preprints202009.0085.v1

method has disadvantages: the numerical cost increases with the increase of the control point, and the degree of freedom of shape deformation is fixed. Therefore the deformation has limited representation capacity.

In addition to deformation modeling, establishing of correspondence between shapes is the critical problem of registration. The one-to-one correspondence of the ICP method is sensitive to initial position and shape loss. To determine the many-to-many correspondence point, Chui et al. [33] shown the fuzzy correspondence between the two shapes. The problem of selecting the robust point matching point correspondence was interpreted as a combination of Gaussian mixture model (GMM) and Expectation Maximization [34]. In the GMM model, one point is the centroid of the Gaussian distribution for the points constituting the shape, and the other point is regarded as data to generate [35]. The variations of GMM have different deformation models according to the obtained transformation parameters and a regularization term. For example, regularizing the second derivative of the transformation becomes a thin-plate spline transformation, and regularizing according to the motion coherence theory becomes a coherent point drift transformation [36,37]. Besides, variations of GMM were generalized by the generalized Gaussian radial basis function [38]. To represent the local spatial representation, an L2E estimator is proposed, which creates a robust spare-dense correspondence[39,40].

However, the mixture model requires a high computational cost because it generates a Gaussian distribution as many as the total number of points. Also, each Gaussian distributions share the standard deviation among the points. The mixture model becomes sensitive to noise and shape loss. Especially for coronary arteries, narrow and tangled structures are very challenging to model in 3D+t. This is because the loss of blood vessel morphology is observed in different heartbeats of the same patient by motion artifacts, and geometrical deformation.

In this paper, we propose a 3D+time coronary artery model that can be inferred in real-time according to ECG signals. The proposed hierarchical cage deformation modeling more robustly/accurately register coronary artery models in different cardiac phases. Once the optimal cage control point is obtained that minimizes the shape dissimilarity of the source shape and the target shape, we interpolate the shape control point to build a continuous 3D+t model. Besides, a modified hyper-elastic regularization term prevents the mesh degeneration problems that may occur during the control point optimization step.

The contribution of the proposed method consists of followings:

1. A hierarchical deformation method to perform robust shape registration even incomplete coronary artery, models
2. A rapid shape interpolation that makes enable restoring small and complex geometry on time-varying coronary artery model
3. The modified hyper-elastic regularization prevents mesh degeneration while shape registration
4. Evaluation of the proposed method using retrospective data for eight patient in qualitatively and quantitatively. The overall structure of the proposed method is shown in figure 1.

2. Pre-processing ECG-gated 4D CT images

In this study, we reconstructed CTA volumes for eight patients at 0% to 95% intervals at 5% intervals between the RR peaks of the heart rate. We took the volumes using a 256-slice multi-detector CT scanner (BRILLIANCE ICT 256 SLICE, Philips Healthcare) at the Cardiovascular Center of Seoul National University Bundang Hospital. This retrospective study was approved by the Institutional Review Board of Seoul National University Bundang Hospital (IRB No. B-2009-637-103).

The cross-sectional size of the image was 512×512 pixels, the average number of slices in the Z-axis direction was 298. The volume voxel resolution was 0.35×0.35×0.45. The left ascending and circumflex coronary arteries were segmented using ITK-Snap software[41]. The segmented arteries have been converted to mesh models through Poisson surface reconstruction, and the average number of nodes was 10638. We selected 75% phase mesh models as templates because left ascending and

Preprints (www.preprints.org) | NOT PEER-REVIEWED | Posted: 4 September 2020 doi:10.20944/preprints202009.0085.v1

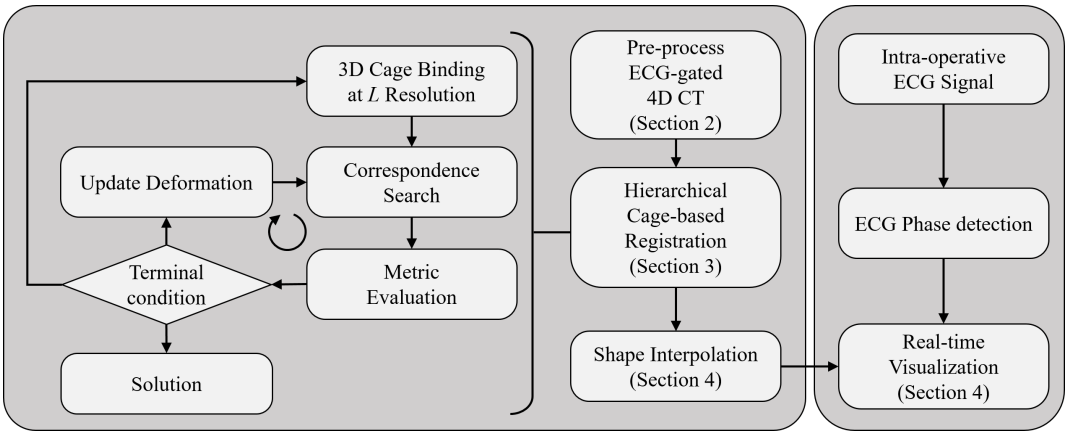

Figure 1. General framework of the proposed method.

circumflex coronary arteries are most clearly observed at a 75% phase [42]. For example, figure 2 shows the models of the template and other phases.

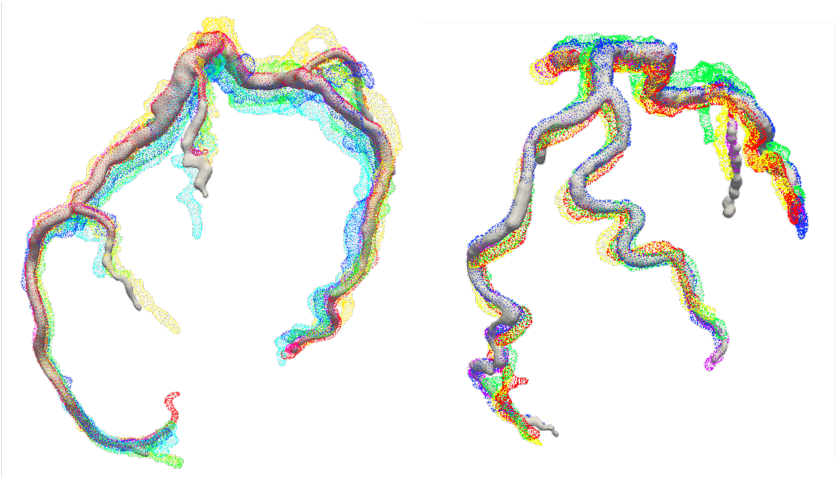

Figure 2. Left ascending and circumflex coronary arteries of patient 1 (left) and 2(right). The template phase model is white solid model, and the other phases are colored points.

3. Hierarchical cage-based shape registration method

In this section, we address the non-rigid registration method to find optimal deformation between coronary artery models. This section is organized as followings, (1) Shape representation and registration problems; (2) Gradient descent for shape control point optimization ; (3) Multi-Resolution Cage Deformation Representation; (4) Diffeomorphism supported by hyper-elasticity regularization;

3.1. Shape representation and registration problems

This section provides basic concepts of representation and registration of shapes. Let the shape V be a $V = \{v_i | v_i \in \mathbb{R}^3, i = 0, \ldots, n-1\}$, which contains n number of vertices. If the shapes V_s and V_t be the source and target shape, respectively, the registration problem is to find an optimal transformation that minimizes the dissimilarity between shapes. Here, an arbitrary transformation T map the source shape V_s to the target shape V_t. Through the optimization process, an optimal transformation parameters x^* minimize disparity measure as following;

$$x^* = \arg\min_x d(T(x) \circ V_s, V_t) \tag{1}$$

Preprints (www.preprints.org) | NOT PEER-REVIEWED | Posted: 4 September 2020 doi:10.20944/preprints202009.0085.v1

The transformation T is a mapping that

$$T : V_s \rightarrow \bar{V} = V_s + U(V_s, x) \tag{2}$$

, where $\bar{V}$ is deformed shape, x is local deformation parameters, and $U(V, x)$ is vertex-wise mapping.

The shape transformation T may be represented through the modification of coarse cage mesh that envelopes the source shape. Let a region Ω be a bound of shape V_s in 3D. The sub-region Ω_r is a part of subdivisions of Ω, where $\Omega = \bigcup_{\forall r} \Omega_r$ and $\Omega_i \cap \Omega j = \emptyset, i \neq j$. If we create the $m \times m \times m$ regular lattice grid on the region Ω, the subdivisions of Ω contain $(m-1)^3$ numbers of control vertices m^3 number of sub-regions. Hereby, the sub-region Ω_r is defined as an 8-point cuboid. The 8-corner points of Ω_r is given as $P_r = \{p_i | p_i \in \mathbb{R}^3, i = 0, \ldots, 7\}$. The linear combination of cage control points and their local coordinate represent the vertices of shape V_s. If the vertex $v \subset \Omega_r$, then the representation of vertex by sub-region control point is given as below;

$$v = F(v; P_r) = \sum_{i=0}^{7} \varphi_i(v) p_i \tag{3}$$

where the ϕ_i is a trilinear shape function for assigning local coordinates, such as

$$\begin{aligned}
\varphi_0(v_x, v_y, v_z) &= (1 - v_x)(1 - v_y)(1 - v_z)/8 \\
\varphi_1(v_x, v_y, v_z) &= (1 + v_x)(1 - v_y)(1 - v_z)/8 \\
\varphi_2(v_x, v_y, v_z) &= (1 + v_x)(1 + v_y)(1 - v_z)/8 \\
\varphi_3(v_x, v_y, v_z) &= (1 - v_x)(1 + v_y)(1 - v_z)/8 \\
\varphi_4(v_x, v_y, v_z) &= (1 - v_x)(1 - v_y)(1 + v_z)/8 \\
\varphi_5(v_x, v_y, v_z) &= (1 + v_x)(1 - v_y)(1 + v_z)/8 \\
\varphi_6(v_x, v_y, v_z) &= (1 + v_x)(1 + v_y)(1 + v_z)/8 \\
\varphi_7(v_x, v_y, v_z) &= (1 - v_x)(1 + v_y)(1 + v_z)/8
\end{aligned} \tag{4}$$

From the previous definition of cage representation, the motion of vertex v in the direction to $\bar{v}$ is given as following;

$$\begin{aligned}
u(v, P_r) &= \bar{v} - v \\
&= \sum_{i=0}^{7} \varphi_i(v)(p_i + \partial p_i) - \sum_{i=0}^{7} \varphi_i(v) p_i \\
&= \sum_{i=0}^{7} \varphi_i(v) \partial p_i
\end{aligned}$$

, where $u(v, x)$ is a motion of vertex v and ∂p_i is motion of control point p_i. Therefore, the shape deformation is only depending on the change of control points as figure 3. Therefore, the parameter of the cage representation of transformation T is given as following;

$$x = \{\partial p_i | \partial p_i \in \mathbb{R}^3, i = 0, \ldots, 7\} \tag{5}$$

Preprints (www.preprints.org) | NOT PEER-REVIEWED | Posted: 4 September 2020 doi:10.20944/preprints202009.0085.v1

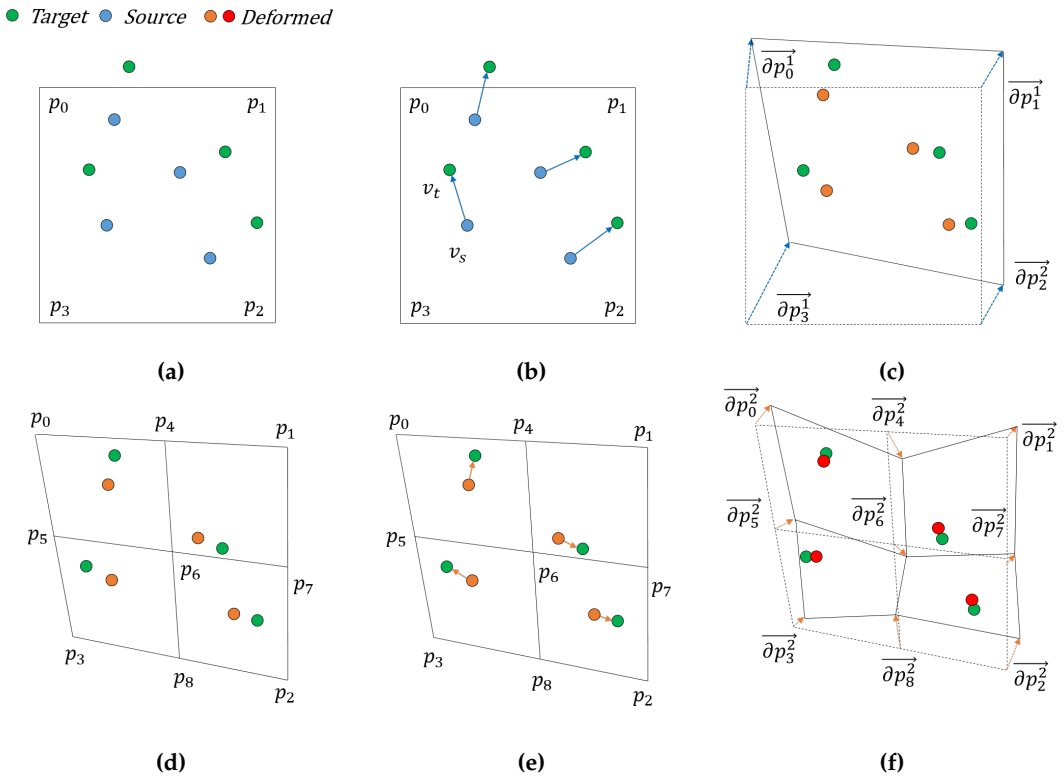

Figure 3. The hierarchical registration in different deformation depth. (a)-(c) Level 1, (d)-(f) Level 2 registration. Figure (a),(d) show cage partitioning in different levels. Figure (b),(e) are correspondence searching, and figure (c),(e) are gradient descent based deformation update, respectively.

3.2. Gradient descent for shape control point optimization

The optimization of the transformation is defined as a process of minimization of a metric. If we set the disparity measure as a squared Euclidean distance between correspondence pair, then

$$d(v_s, v_s, P) = \|T(P) \circ v_s - v_t\|^2 \tag{6}$$

$$= \|F(v_s; P) - v_t\|^2 \tag{7}$$

$$= \| \sum_{i=0}^{7} \varphi_i(v_s) p_i - v_t\|^2 \tag{8}$$

where $v_s \in V_s$, $v_t \in V_t$ and v_s, v_t is correspondence pair.

Thus, the gradient can be denoted as the sum of the difference vector of the corresponding pair that multiplied by the weight of each control point. Therefore, the partial derivative of disparity measure for one of cage control point $p_i = (p_{ix}, p_{iy}, p_{iz})$ is

$$\frac{\partial}{\partial p_i} d(v_s, v_t, P) = \frac{\partial}{\partial p_i} \|v_s - v_t\|^2 \tag{9}$$

$$= 2\|v_s - v_t\| \cdot \frac{\partial}{\partial p_i} \| \sum_{i=0}^{7} \varphi_i(v_s) p_i - v_t\| \tag{10}$$

$$= 2\|v_s - v_t\| \cdot \varphi_i(v_s) \tag{11}$$

Preprints (www.preprints.org) | NOT PEER-REVIEWED | Posted: 4 September 2020 doi:10.20944/preprints202009.0085.v1

The Jacobian matrix for disparity measure of one correspondence pair is

$$\frac{\partial}{\partial P} d(v_s, v_t, P) = \begin{bmatrix} \frac{\partial}{\partial p_0} d(v_s, v_t, P) \\ \frac{\partial}{\partial p_1} d(v_s, v_t, P) \\ \vdots \\ \frac{\partial}{\partial p_m} d(v_s, v_t, P) \end{bmatrix} = \begin{bmatrix} \partial p_{0x} & \partial p_{0y} & \partial p_{0z} \\ \partial p_{1x} & \partial p_{1y} & \partial p_{1z} \\ & \vdots & \\ \partial p_{mx} & \partial p_{my} & \partial p_{mz} \end{bmatrix} \tag{12}$$

The update of cage control points is the distribution of the differences corresponding pairs, which are the vectors from source to targets generated inside the sub-regions Ω_r. At this time, the robust correspondence selection potentially supports the update of cage control points. To establish the correspondence pair robustly, we constraints the correspondence searching process using orientation filtering as following;

$$\{v_s, v_t\} = \begin{cases} \text{Paired}, & \text{if } \theta(\vec{n}_s, \vec{n}_t) < \theta_{\text{Threshold}} \\ \text{Not paired}, & \text{otherwise} \end{cases} \tag{13}$$

, where $\theta(\cdot, \cdot)$ is angle between two vector, and $\vec{n}_s$, $\vec{n}_t$ are vertex normal of v_s and v_t, respectively. We set $\theta_{\text{Threshold}} = 30^\circ$. The Jacobian matrix for sum of squared Euclidean distance is

$$\sum_{\{v_s, v_t\} \in \forall I_{V_s}} \frac{\partial}{\partial P} d(v_s, v_t, P) = \begin{bmatrix} \sum \partial p_0 \\ \sum \partial p_1 \\ \vdots \\ \sum \partial p_m \end{bmatrix} \tag{14}$$

, where I_{V_s} is the set of correspondence pair.

3.3. Multi-Resolution Cage Deformation Representation

In this section, we present a cage deformation method using multi-resolution to represent a gradual deformation. In the registration process, the resolution of the cage determines the degree of freedom of shape deformation. As increasing the resolution of the cage, the deformation model can represent a more detailed shape change. However, the dense cage has a disadvantage that can lose the overall shape. A method of maintaining local shape features through multi-resolution or hierarchical data structures is used as a complementary method.

We assumed the generation of the cage based on the regular lattice grid. The primitive shape of the cage obtained from the lattice structure is a cube with 8 vertices and 6 quadrilateral faces, and the points inside the cage can be represented as linear combinations of cage control vertices. As shown in figure 3, the cage can be partitioned into the inner sub-regions, and the control points of this sub-region can be created from the control points of the outer region. If we denote the vertex v using cage control points P^n at the deformation depth n as following;

$$v = F(v; P^n) = \sum_{i=0}^{7} \varphi_i(v) p_i^n \tag{15}$$

, where p_i^n is i-th cage control point at deformation depth n. If we recursively acquire the sub-region of the region Ω that surrounds the source model, we can denote the higher-level control points using the lower level control points. Generalized formula presents the corner points of the subdivision, which is recursively described in the multi-resolution process as below;

$$P^m = F(P^m; P^n) = \sum_{i=0}^{7} \varphi_i(P^m) p_i^n \tag{16}$$

Preprints (www.preprints.org) | NOT PEER-REVIEWED | Posted: 4 September 2020 doi:10.20944/preprints202009.0085.v1

, where $m > n$ and $m, n \in \mathbb{N}$. Thus, if we represent the shape using a chain of cage deformations, the deformed vertex $\bar{v}$ with respect to the level n deformation is

$$\bar{v} = F(v; P^n, \partial P^n) = \sum_{i=0}^{7} \varphi_i(v)(p_i^n + \partial p_i^n) \tag{17}$$

Similarly, the deformed vertex $\bar{v}$ by level n deformation after level $n-1$ deformation is

$$\begin{aligned} \bar{v} &= F(v; P^n, P^{n-1}) \\ &= \sum_{i=0}^{7} \varphi_i(v)(\sum_{j=0}^{7} \varphi_j(p_i)(p_j^{n-1} + \partial p_j^{n-1}) + \partial p_i^n) \end{aligned} \tag{18}$$

To cooperate with the gradient descent, we reformulate the $\frac{\partial}{\partial p_i} d(v_s, v_t, P)$ as multi-resolution process. The partial derivative of given cost function at $n-1$-th level is given as below;

$$\begin{aligned} \frac{\partial}{\partial p_i^{n-1}} d(v_s, v_t, P) &= \frac{\partial}{\partial p_i^{n-1}} \| \sum_{i=0}^{7} \varphi_i(v_s) p_i^n - v_t \|^2 \\ &= \frac{\partial}{\partial p_i^{n-1}} \| \sum_{i=0}^{7} \varphi_i(v_s) \sum_{j=0}^{7} \varphi_j(p_i^n) p_j^{n-1} - v_t \|^2 \\ &= 2\|v_s - v_t\| \cdot \| \sum_{i=0}^{7} \varphi_i(v_s) \varphi_j(p_i^n) \| \end{aligned} \tag{19}$$

The modification of control point ∂p_i in the multi-resolution of cage sub-division is

$$\partial p_i = \partial p_i^n + \partial p_i^{n-1} + \cdots + \partial p_i^1 \tag{20}$$

3.4. Diffeomorphism supported by hyper-elasticity regularization

Although hierarchical cage deformation recursively represents shape deformation to avoid local minimums, the dense cages possibly lead to more cage degeneration. Therefore, it needs the appropriate regularization process when applying hierarchical transformations. To have plausible deformation, we impart hyper-elastic regularization that prevents unexpected partial deformation. We utilized and modified the study of Burger et al. [20] that can be easily extended to the cage deformation settings. As shown in figure 4, the 24 sub-regions of the cage are defined using corner points p_i and seven auxiliary points, which are volume points p_V and face points p_F. Tetrahedral sub-regions are defined by a span of volume point and face points. Regularization supports the transformation to be diffeomorphism that is reversible and smooth. The hyper-elastic regularization is defined from Burger et al. [20, equation 2.6];

$$S^{hyper}(x) = \int \alpha_1 \eta_{vol}(x) + \alpha_2 \eta_{sur}(x) + \alpha_3 \eta_{len}(x) d\Omega \tag{21}$$

where α_i are balancing parameter. Functions η_{vol},η_{sur},and η_{len} penalizes the change of volume, surface, and length, respectively. Here, we set the balancing parameter as 10.0 for all experiments. Burger et al.[20] utilized the average points to delineate the volume point p_V and six face points p_F for each. However, if the cage is concave due to large deformation, the face and volume points are not maintained inside the cage as figure 4. As a result, the functions η_{vol} and η_{sur} may have a negative value, which leads to the failure of the gradient descent.

To achieve robust regularization, we define the face and volume vertices of each cage to have the same sub-area and sub-volume inside of the cage. We assume that the face point $p_F = (p_{F_x}, p_{F_y}, p_{F_z})$ is

Preprints (www.preprints.org) | NOT PEER-REVIEWED | Posted: 4 September 2020 doi:10.20944/preprints202009.0085.v1

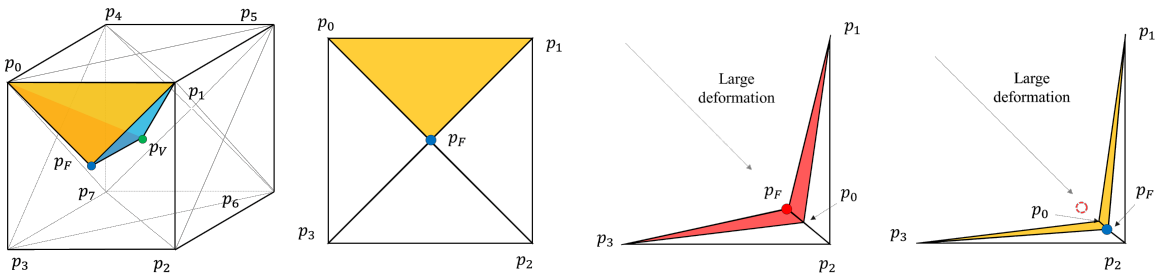

(a) **(b)** **(c)** **(d)**

Figure 4. The cage sub-division for hyper-elastic regularization. (a) A tetrahedral sub-division of 3D cage volume that is a span of face point(blue) and volume point(green), (b) sub-division of cage face, (c) the average point(red) locating outside of the cage and their negative areas(red triangles), and (d) the equal-area point(blue) locating inside of cage despite large deformation and their positive areas(yellow triangles).

located inside the quadrilateral, the position p_F of the points dividing the areas $\triangle p_0 p_1 p_F$, $\triangle p_1 p_2 p_F$, $\triangle p_2 p_3 p_F$, and $\triangle p_3 p_0 p_F$, is defined as follows;

$$\triangle p_i p_{i+1} p_F = (p_{i+1} - p_i) \times (p_F - p_i)/2 = [p_{i+1} - p_i]_\times (p_F - p_i)/2 \tag{22}$$

where $i = \{0, 1, 2, 3\}$. The least square solution of above conditions for all triangles is

$$\begin{bmatrix} [p_1 - p_0]_\times \\ [p_2 - p_1]_\times \\ [p_3 - p_2]_\times \\ [p_0 - p_3]_\times \end{bmatrix} \begin{bmatrix} p_{F_x} \\ p_{F_y} \\ p_{F_z} \end{bmatrix} = \begin{bmatrix} [p_1]_\times p_0 \\ [p_2]_\times p_1 \\ [p_3]_\times p_2 \\ [p_1 0]_\times p_3 \end{bmatrix} \tag{23}$$

Similar to the face point, we assume the volume point to locate inside the hexahedron. The volume point $p_V = (p_{V_x}, p_{V_y}, p_{V_z})$ partitions 24 sub-tetrahedron of the cage. The volume of single tetrahedron is given as

$$V_{p_{i,j} p_{i+1,j} p_{F_j}} = (p_{i+1,j} - p_{i,j}) \times (p_{F_j} - p_{i,j}) \cdot (p_V - p_{i,j})/6 \tag{24}$$

, where p_{F_j} is j-th face point of hexahedron and $p_{i,j}$ is i-th corner point of j-th face.

The volume point p_V is obtained by solving the least square problem as follows;

$$\begin{bmatrix} [p_{1,0} - p_{0,0}]_\times p_{F_0} - [p_{1,0}]_\times p_{0,0} \\ [p_{2,0} - p_{1,0}]_\times p_{F_0} - [p_{2,0}]_\times p_{1,0} \\ [p_{3,0} - p_{2,0}]_\times p_{F_0} - [p_{3,0}]_\times p_{2,0} \\ [p_{0,0} - p_{3,0}]_\times p_{F_0} - [p_{0,0}]_\times p_{3,0} \\ \vdots \\ [p_{0,5} - p_{3,5}]_\times p_{F_5} - [p_{0,5}]_\times p_{3,5} \end{bmatrix} \begin{bmatrix} p_{V_x} \\ p_{V_y} \\ p_{V_z} \end{bmatrix} = \begin{bmatrix} -[p_{1,0}]_\times p_{0,0} \cdot p_{F_0} \\ -[p_{2,0}]_\times p_{1,0} \cdot p_{F_0} \\ -[p_{3,0}]_\times p_{2,0} \cdot p_{F_0} \\ -[p_{0,0}]_\times p_{3,0} \cdot p_{F_0} \\ \vdots \\ -[p_{0,5}]_\times p_{3,5} \cdot p_{F_5} \end{bmatrix} \tag{25}$$

The robust face/volume points improve the numerical stability of the cage deformation. The cost function is a combination of dissimilarity measurement and regularization.

4. Interpolation of shape control points

In this section, we introduce the shape interpolation and restoration for real-time usage of the 3D+t coronary artery model. According to equation 3, the shape of the coronary artery relies on the location of the control points. Therefore, as we derive the intermediate positions of control points among cardiac phases, the corresponding shape is restored. To interpolate the positions of control points, we

Preprints (www.preprints.org) | NOT PEER-REVIEWED | Posted: 4 September 2020 doi:10.20944/preprints202009.0085.v1

consider a set of control point at the k-th phase as a vector P_k, such that $P_k = \{p_0, p_1, \ldots, p_{n-2}, p_{n-1}\}$, where $p_i \in \mathbb{R}^3$ and n is the number of cage control points. From the registration results, we interpolate the given sets of control points using periodic cubic spline interpolation [43] due to the natures of the heart's cyclic motion. The number of knots is the same as the number of reconstruction from 4D CTA.

Let a phase-vary vector $S(t) = \{s_0(t), \ldots, s_{n-1}(t)\}$ be the set of interpolated control points, where $s_i(t)$ is i-th control spline for the cardiac phases t. The spline vector $S(t)$ has C^2 continuity with respect to the phase t. The spline function $S(t)$ maps phase t to set of cage control points, such as $S : \mathbb{R} \to \mathbb{R}^{3\times n}$. Then, the vertices of shape are restored using below;

$$v(t) = F(v; S(t)) = \sum_{i \in I_V} \varphi_i(v) s_i(t) \tag{26}$$

5. Evaluations and Results

In this section, we evaluate the proposed method qualitatively and quantitatively on data from eight patients. The proposed method was tested on a workstation, Intel(R) Xeon (R) W-2133 CPU@3.60GHz, 32-GB ram. We partially multi-threaded the computation of cost function measurements using OpenMp[44] and Thread building block[45] during the optimization process. The proposed method and comparison target methods are written in C++.

5.1. Quantitative evaluations

In the quantitative evaluation of non-rigid registration, we used the metrics, such that 1)the closest point-mesh Euclidean distance(ED) from the target model to the matching result, and 2)the dice coefficient(DC) obtained from the mesh boolean operation. Since we set the number of iterations to 300/maxDepth for each depth, the total number of iteration for different max depths set to be the same.

5.1.1. Trade-off between deformation depth and computation time

Method	Cage Resolution	Computation Time (sec)	Average distance (mm)	Dice Coefficient
HierCage	[1, 1, 1]	21.73	0.668 ± 0.255	0.655 ± 0.096
HierCage	[2, 2, 2]	23.05	0.597 ± 0.234	0.696 ± 0.077
HierCage	[3, 3, 3]	22.91	0.566 ± 0.227	0.721 ± 0.068
HierCage	***[4, 4, 4]***	***23.52***	***0.543 ± 0.222***	***0.735 ± 0.064***
HierCage	[5, 5, 5]	33.00	0.534 ± 0.221	0.741 ± 0.064
GRBF_KC	[4, 4, 4]	40.99	0.615 ± 0.218	0.666 ± 0.088
GRBF_L2	[4, 4, 4]	40.92	0.600 ± 0.207	0.671 ± 0.084
TPS_KC	[4, 4, 4]	33.00	0.553 ± 0.191	0.681 ± 0.080
TPS_L2	[4, 4, 4]	***32.21***	***0.530 ± 0.178***	***0.690 ± 0.075***

Table 1. The trade-off between computation time and accuracy

Firstly, we observed the trade-off between the degrees of freedom of deformation and computation time. As shown in table 1, we compared the different depths of deformation incrementally from 1 to 5. As shown in figure 5, the ED and DC become worsen as the phases are far from the template phase. Since the shape of the blood vessel is a thin tube shape, the ED and DC values become noticeably deteriorated with a slight movement. As the deformation depth increases, the ED values gradually decreased, and the DC values increased more prominently, both the metrics become flattened for the other cardiac phases. The metrics converged after deformation depth 4. The comparison results for the other patients are in A.1 and A.2.

Preprints (www.preprints.org) | NOT PEER-REVIEWED | Posted: 4 September 2020 doi:10.20944/preprints202009.0085.v1

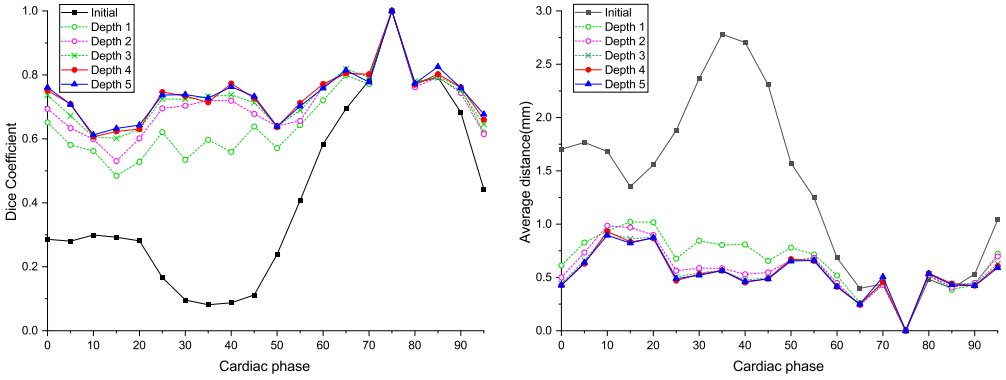

(a) **(b)**

Figure 5. Effect of cage deformation depth for patient 1 at the different cardiac phases. (a) dice coefficients, (b) average distance from target to deformed model.

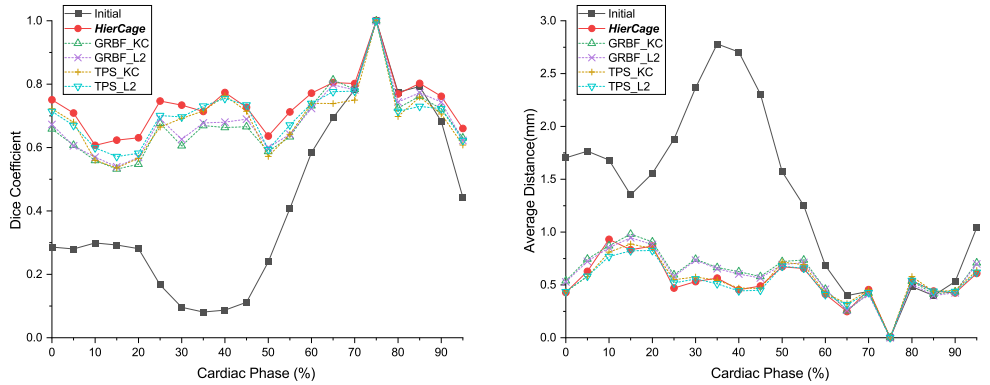

(a) **(b)**

Figure 6. Comparison of other algorithms for patient 1 at the different cardiac phases. (a) dice coefficients, (b) average distance from target to deformed model.

5.1.2. Comparison with other methods

In the second experiment, the proposed registration method's performance was compared with other non-rigid matching algorithms. As the comparison target of non-rigid registration, we selected the variations of GMM methods, which are the combinations of a deformation model and cost function. The deformation models are Thin-plate spline(TPS) and Generalized Radial basis function(GRBF), the cost functions are kernel correlation (KC) or L_2 distance. The comparison targets used L-BFGS-B as an optimization method.

For comparison, each deformation model has the same number of deformation control points. Since the convergence of accuracy from the previous analysis, we set the number of grid and control points as 16x16x16 and 4913, respectively. As shown in figure 6, the proposed method shows equal or better accuracy and has faster than the other methods. Although the ED metrics show a similar trend compared with other methods, it showed a significant improvement in DC. The comparison results for the other patients are in A.3 and A.4.

5.1.3. Interpolation Accuracy

In this section, we evaluated the accuracy of the interpolated 3D+t coronary artery models by comparing them with the segmented models. The proposed method creates the smooth and non-degenerated 3D model by interpolating the cage control points over sampled cardiac phases, as shown in figure 8. Our data-sets are evenly reconstructed from 4D CT within R-R peak (5% sampling interval). Thus we have 20 number of keyframes($V_{0\%}$, $V_{5\%}$, ..., $V_{95\%}$). To evaluate the effect of the

Preprints (www.preprints.org) | NOT PEER-REVIEWED | Posted: 4 September 2020 doi:10.20944/preprints202009.0085.v1

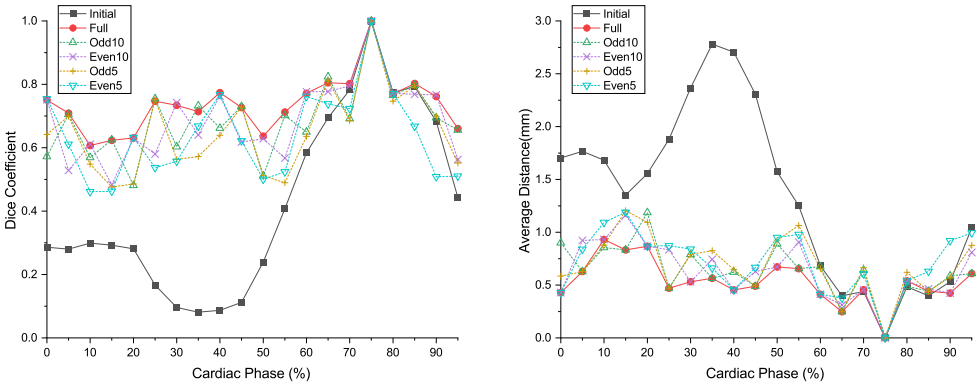

(a) **(b)**

Figure 7. Comparison of interpolation sampling for patient 1 at the different cardiac phases. (a) dice coefficients, (b) average distance from target to deformed model.

(a) **(b)** **(c)** **(d)**

Figure 8. The comparison of registered model and interpolated model for patient 5. (a) Template (green) and 40% coronary artery(red), (b) registered model(blue), (c) interpolated model(yellow), and (d) comparison of registered model and interpolated model.

sampling of cardiac phases, we choose the phase sets from the given 20 number of keyframes as followings; (1) Odd 10 : [5,15,25,... ,85,95], (2) Even 10: [0,10,20,... ,80,90], (3) Odd 5 : [5,25,45,65,85], and (4) Even 5 : [0,20,40,60,80]. Figure 7 shows the differences among the phase selection. Although the sampled phase became sparse, the DC of the interpolated result showed that the results have a lower bound. The ED still showed a flatten value when compared to the before registration. The comparison results for the other patients are in A.5 and A.6.

5.2. Qualitative evaluations

In the qualitative evaluation, the role in the visualization effect of hyper-elastic regularization, geometrical comparison with other algorithms, comparison of the matching result and interpolation result model, and the limitations of the interpolation model were investigated.

5.2.1. The effect of hyper-elastic regularization and hierarchical deformation

High order deformation models often converge to a local minimum, which may look visually implausible. Figure 9.(a)-(b) show the example of shape shrinkage when the target model contains loss of shape. The hyper-elastic regularization constraints on the shape preservation, which provides a plausible result as figure 9.(c)-(d).

When compared with other algorithms, figure 10 shows the example that the shape registration is defective at the excessively deformed and the twisted part. Because the registration process converges to the local minimum, the deformation model represents the further details of local deformation. On the other hand, Hierarchical cage deformation gradually acquires an optimal solution to avoid

Preprints (www.preprints.org) | NOT PEER-REVIEWED | Posted: 4 September 2020 doi:10.20944/preprints202009.0085.v1

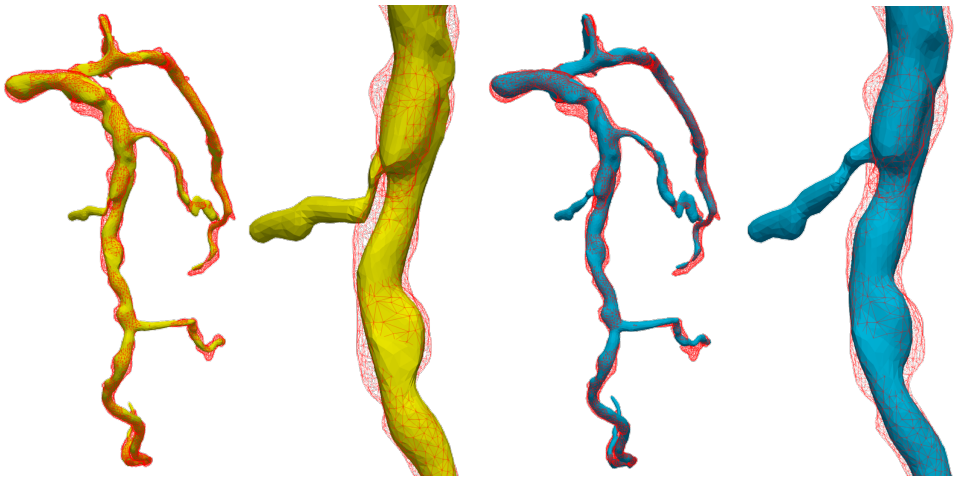

(a) (b) (c) (d)

Figure 9. The effect of modified hyper-elastic regularization. We aligned source model to target model(red) that contains loss of branch. The figure show effects of (a)-(b) without regularization(yellow) and (c)-(d) with regularization(blue).

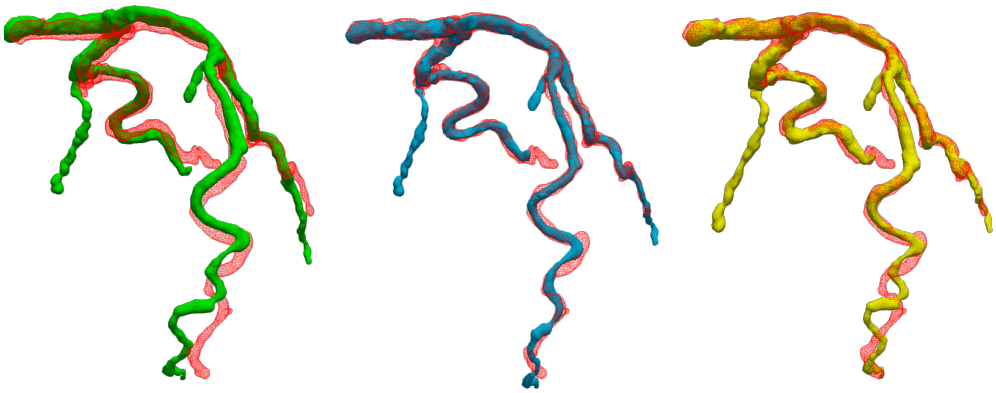

(a) (b) (c)

Figure 10. The qualitative comparison of GMM and the proposed method. (a)Intial template model(green) and target coronary artery(red), (b) result of the proposed method(blue), and (c) result of Gaussian mixture modeling with TPS+L_2(yellow)

local minimums from coarse to dense resolution, as shown in figure 11. In this process, a low degree of freedom deformation is an initial value of the deformation in the next step. Therefore the local minimum can be avoided more efficiently.

5.2.2. The representation power of interpolated model

The proposed shape interpolation method may have a limited representation for intermediate shape. This limited shape representation is due to the recurring shape of the adjacent phases. We observed that the shape interpolation method restrictively delineates the intermediate shape. The shapes of the neighboring phases to the target phase resemble each other, but the target shape and the neighbor shapes are considerably different as figure 12.(e).

6. Discussion and Conclusion

In this paper, we proposed a method of generating a 3D + time vessel model that can be used in real-time from 4D CT images. Our purpose is to create a 4D vascular model without mesh degeneration, interpolate a model at high speed, and express a more precise shape.

Preprints (www.preprints.org) | NOT PEER-REVIEWED | Posted: 4 September 2020 doi:10.20944/preprints202009.0085.v1

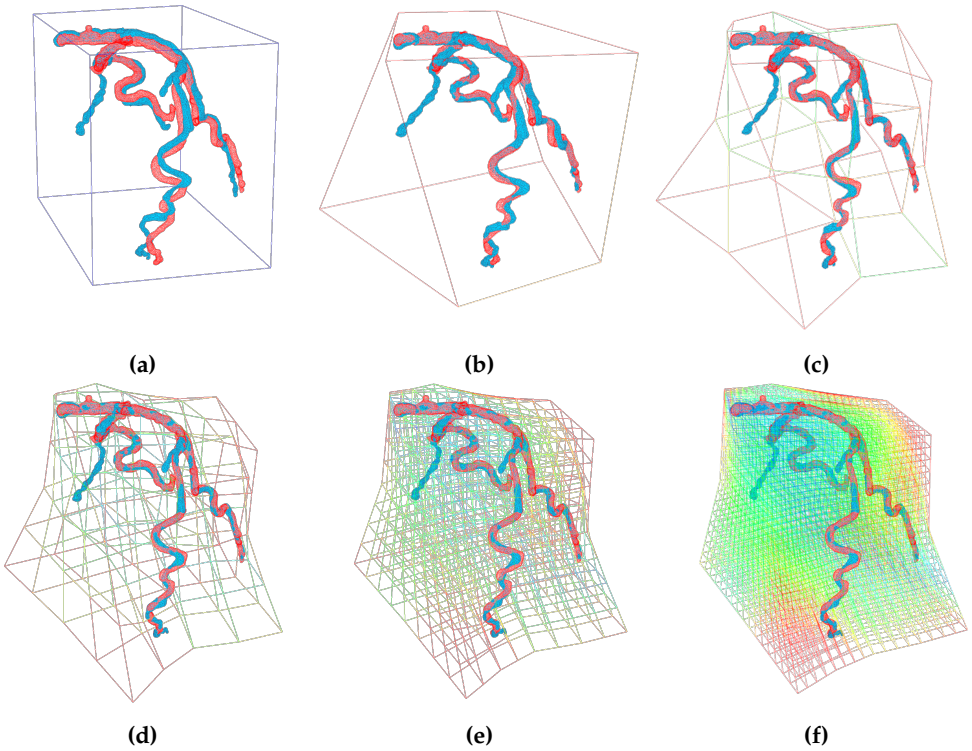

Figure 11. The qualitative comparison of the proposed method while changing the deformation resolution. (a)Initial template model (blue) and target model (red), (b)-(f)the results of registration (blue) at different cage resolutions from [1, 1, 1] to [5, 5, 5], respectively.

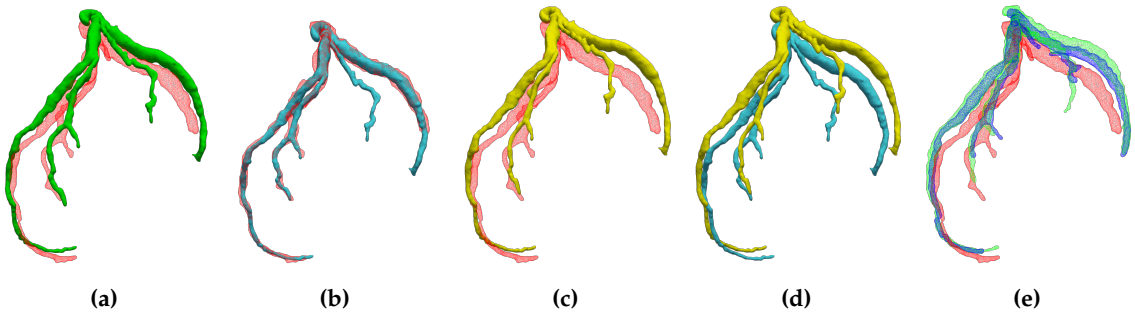

Figure 12. The comparison of registered model and interpolated model for patient 8. (a) Template (green) and 95% coronary artery(red edges), (b) registered model(blue), (c) interpolated model(yellow), (d) comparison of registration interpolation, and (e) comparison of neighboring coronary artery models(90% for dark blue, and 0% for light green).

To create a 4D vascular model, we matched the diastolic coronary artery model with the coronary artery model in other phases through hierarchical cage deformation. During the registration process, hyper-elastic regularization was used as a shape preservation constraint. The shape control points obtained as a result of the registration were interpolated into a cyclic cubic-spline to create a 3D+t model. The shape change depends only on the control points of the cage. The rapid deformation application and the preservation features of the local information act as merits in the shape registration process.

To evaluate the precision of the proposed method, a quantitative and qualitative evaluation was performed on 160 CTA volumes acquired from 8 patients. In the quantitative evaluation:

1. The trade-off between the shape matching accuracy and calculation time according to the hierarchical deformation

 doi:10.20944/preprints202009.0085.v1

2. The comparative evaluation with other methods
3. The accuracy of the shape interpolation model according to the time sampling interval.

In the step of measuring the shape matching precision according to the hierarchical deformation, we observed that the matching precision converged in the 4th step of the hierarchical deformation, and the calculation time was 23.53 seconds on average. In the 5th deformation depth of hierarchical transformation, the matching accuracy slightly increased, but the required time increased by 28.70% to 33.00 seconds. In the hierarchical transformation of the cage creation stage, the control points constituting the cage increased exponentially because a regular grid was used. We obtained the mean distance with precision of a 0.543mm, and standard deviation 0.222 in step 4 of hierarchical transformation, and the Dice coefficient obtained an average 0.754 and a standard deviation 0.064.

When compared with other algorithms, the GMM method requires the creation of a mixture model for each point, so even with the same degree of freedom of transformation, the calculation time is as high as 40 seconds for the GRBF model and 33 seconds for the TPS model. In addition, in the average distance index, TPS_L2 was 0.530mm, which had an error lower than 0.543 of the proposed method, but when comparing the Dice coefficient, TPS_L2 was observed to be 0.690, 0.45 points lower than 0.735, which is the index of the proposed method. The precision of the shape interpolation model was measured with different phase-sampling sets, and the accuracy was worsened when the larger the phases-sampling interval. However, this limitation may be resolved by increase the temporal resolution and cooperate with the other real-time imaging system, such as X-ray angiography and the 4D US.

A qualitative evaluation was performed to support the quantitative evaluation mentioned above and to observe the effect at the visualization stage. In the qualitative evaluation, (1) the effect of modified hyper-elastic regularization and hierarchical transformation, and (2) the limitations in shape interpolation were observed.

When observed the effect of hyper-elastic regularization, the shape was transformed to be visually plausible when hyper-elastic regularization is used. This phenomenon was particularly well seen in the coronary artery model with loss of shape. This is a characteristic obtained by minimizing excessive deformation by robustly obtaining face points and volume points against rapid degeneration of cage mesh due to incorrect correspondence pair. Compared with other non-rigid algorithms, the proposed method was able to cope with the local minimum that occurs during the optimization process by performing the transformation hierarchically better. In particular, it was shown that in the vascular model with an excessive twist, optimal deformation was gradually obtained from low-dimensional deformation.

Therefore, we expect that the proposed 3D+t vascular model, which can be utilized in real-time, can be used for pre-operative blood flow analysis and 2D X-ray-3D shape matching during the intervention. As a limitation of this study, since the deformed model of the proposed model is limited to 3D mesh, blood vessel segmentation is required in phases other than the template model. In a future study, we will conduct a study on a volume-template mesh model matching method that can be applied to volumetric data, including shape loss in order to eliminate unnecessary repetitive processes.

Author Contributions: Conceptualization, Siyeop Yoon, Changhwan Yoon, Eun ju Chun and Deukhee Lee; Data curation, Siyeop Yoon, Changhwan Yoon and Eun ju Chun; Formal analysis, Siyeop Yoon and Deukhee Lee; Funding acquisition, Deukhee Lee; Investigation, Siyeop Yoon; Methodology, Siyeop Yoon and Deukhee Lee; Project administration, Deukhee Lee; Resources, Siyeop Yoon, Changhwan Yoon, Eun ju Chun and Deukhee Lee; Software, Siyeop Yoon; Supervision, Deukhee Lee; Validation, Siyeop Yoon; Visualization, Siyeop Yoon; Writing – original draft, Siyeop Yoon; Writing – review & editing, Siyeop Yoon and Deukhee Lee. All authors have read and agreed to the published version of the manuscript.

Funding: This work was supported by KIST intramural grants (2E30260).

Conflicts of Interest: The authors declare no conflict of interest.

Preprints (www.preprints.org) | NOT PEER-REVIEWED | Posted: 4 September 2020 doi:10.20944/preprints202009.0085.v1

Appendix A. Patient wise evaluations

Appendix A.1. Dice coefficients at different levels of deformation

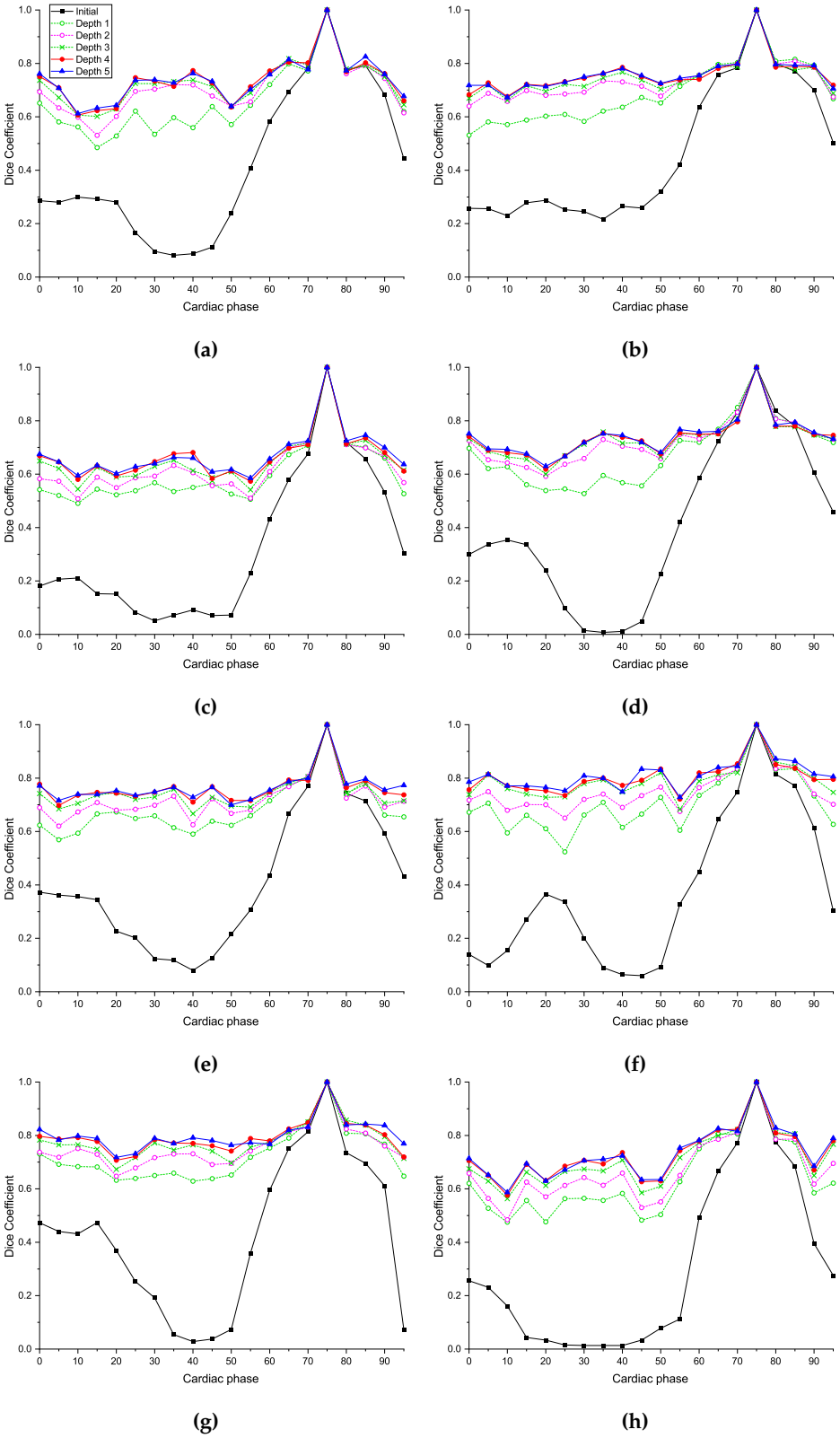

Figure A1. (a)-(h)Dice coefficients at different levels of deformation from patient 1 to patient 8.

Preprints (www.preprints.org) | NOT PEER-REVIEWED | Posted: 4 September 2020 doi:10.20944/preprints202009.0085.v1

Appendix A.2. Average distances at different levels of deformation

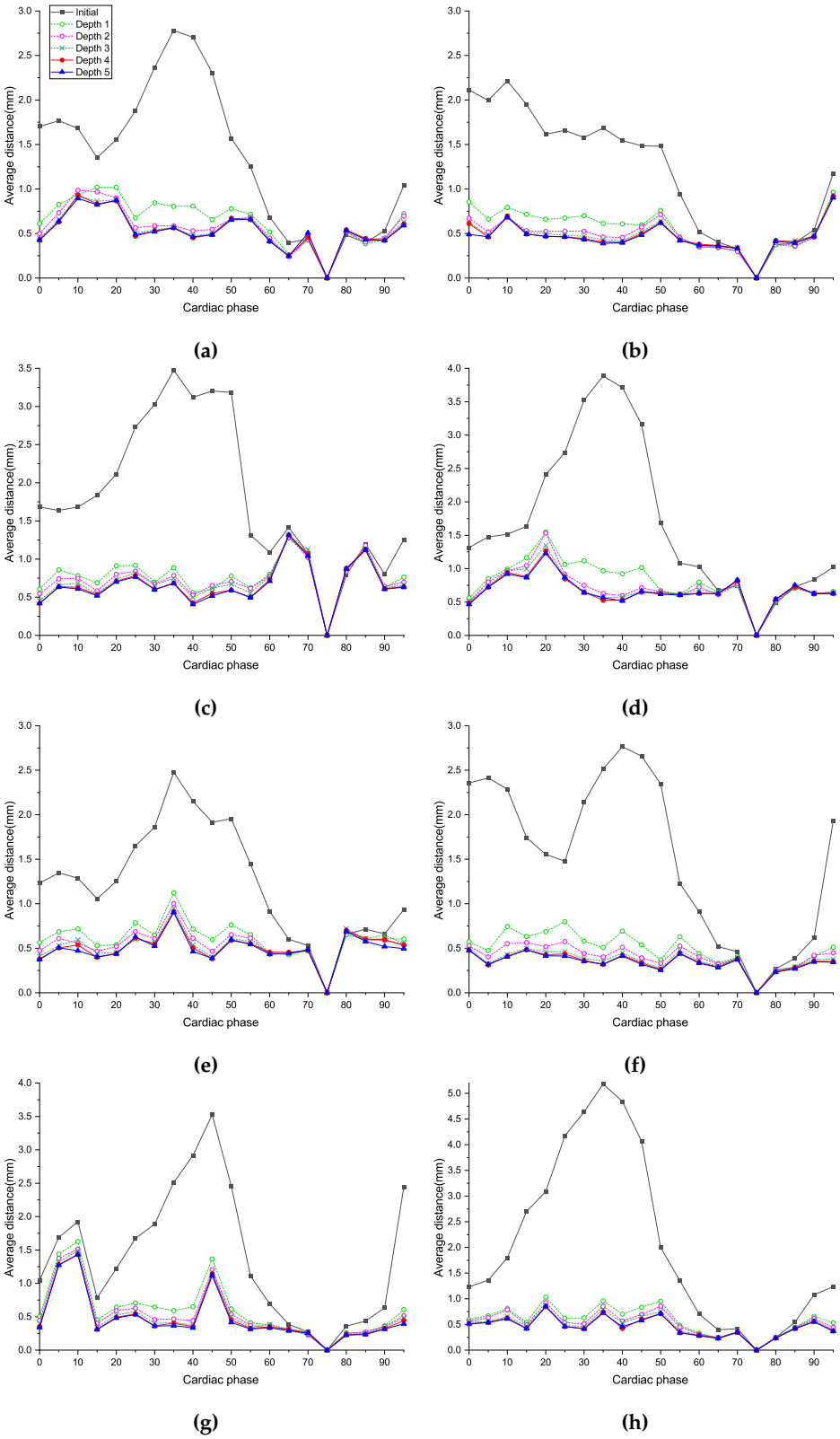

Figure A2. (a)-(h)Average distances between target model to deformed models from patient 1 to patient 8.

Preprints (www.preprints.org) | NOT PEER-REVIEWED | Posted: 4 September 2020 doi:10.20944/preprints202009.0085.v1

Appendix A.3. Dice coefficients for different methods

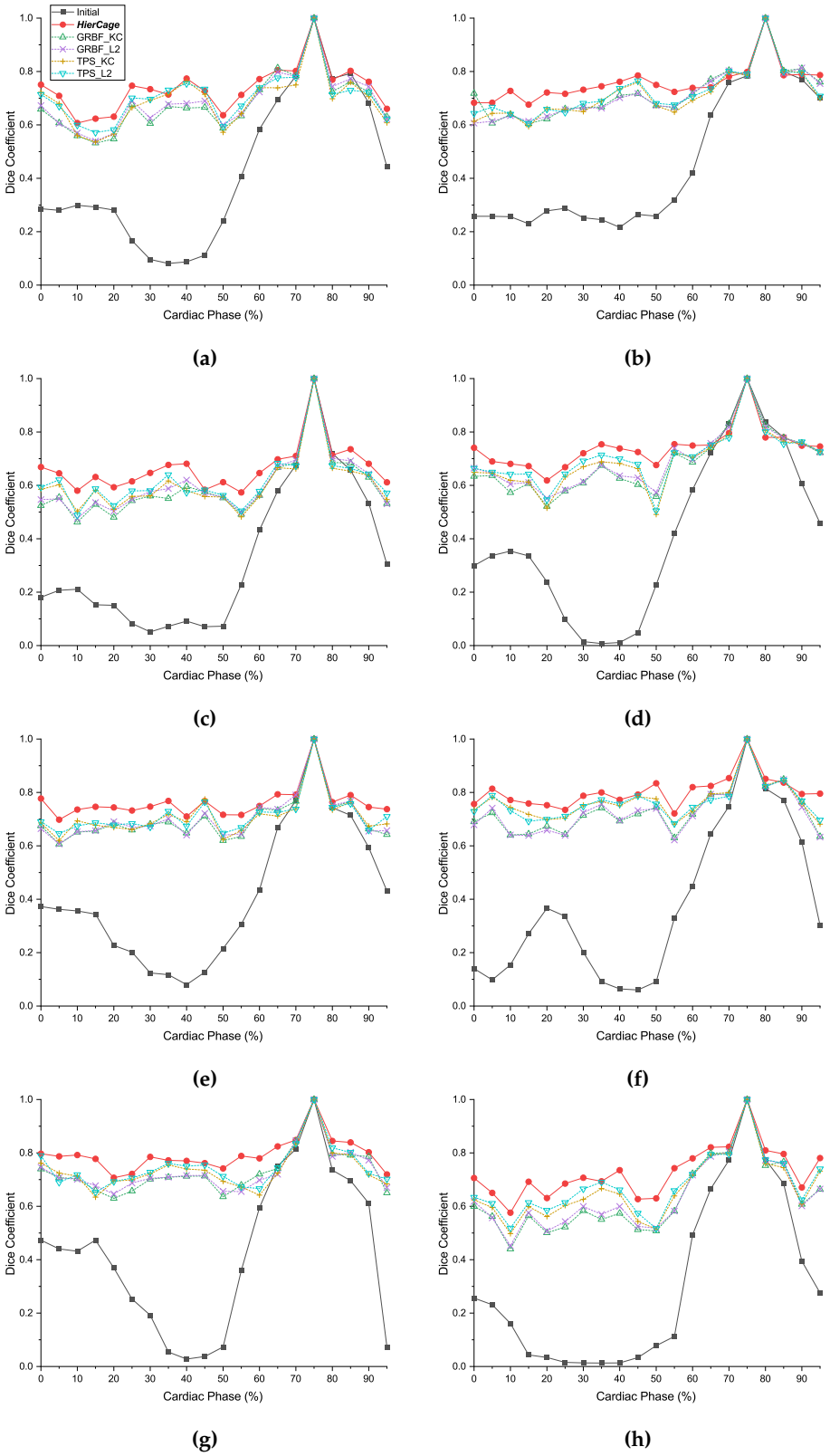

Figure A3. (a)-(h)Dice coefficients between target model to deformed models at the different cardiac phase.

Preprints (www.preprints.org) | NOT PEER-REVIEWED | Posted: 4 September 2020 doi:10.20944/preprints202009.0085.v1

Appendix A.4. Average distances for different methods

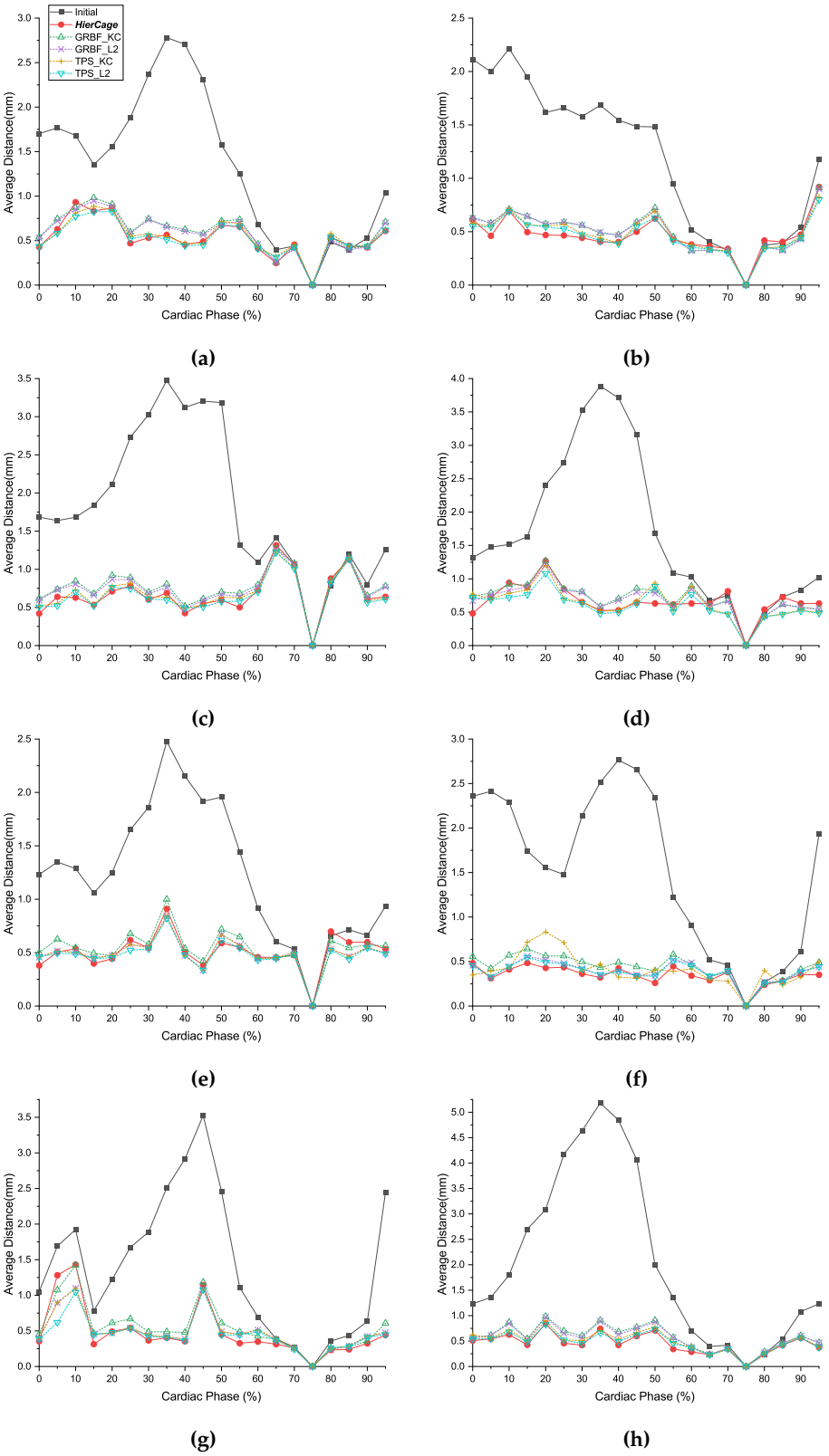

Figure A4. (a)-(h)Average distances between target model to deformed models at the different cardiac phase.

Preprints (www.preprints.org) | NOT PEER-REVIEWED | Posted: 4 September 2020 doi:10.20944/preprints202009.0085.v1

Appendix A.5. Dice coefficients for different phase sampling methods

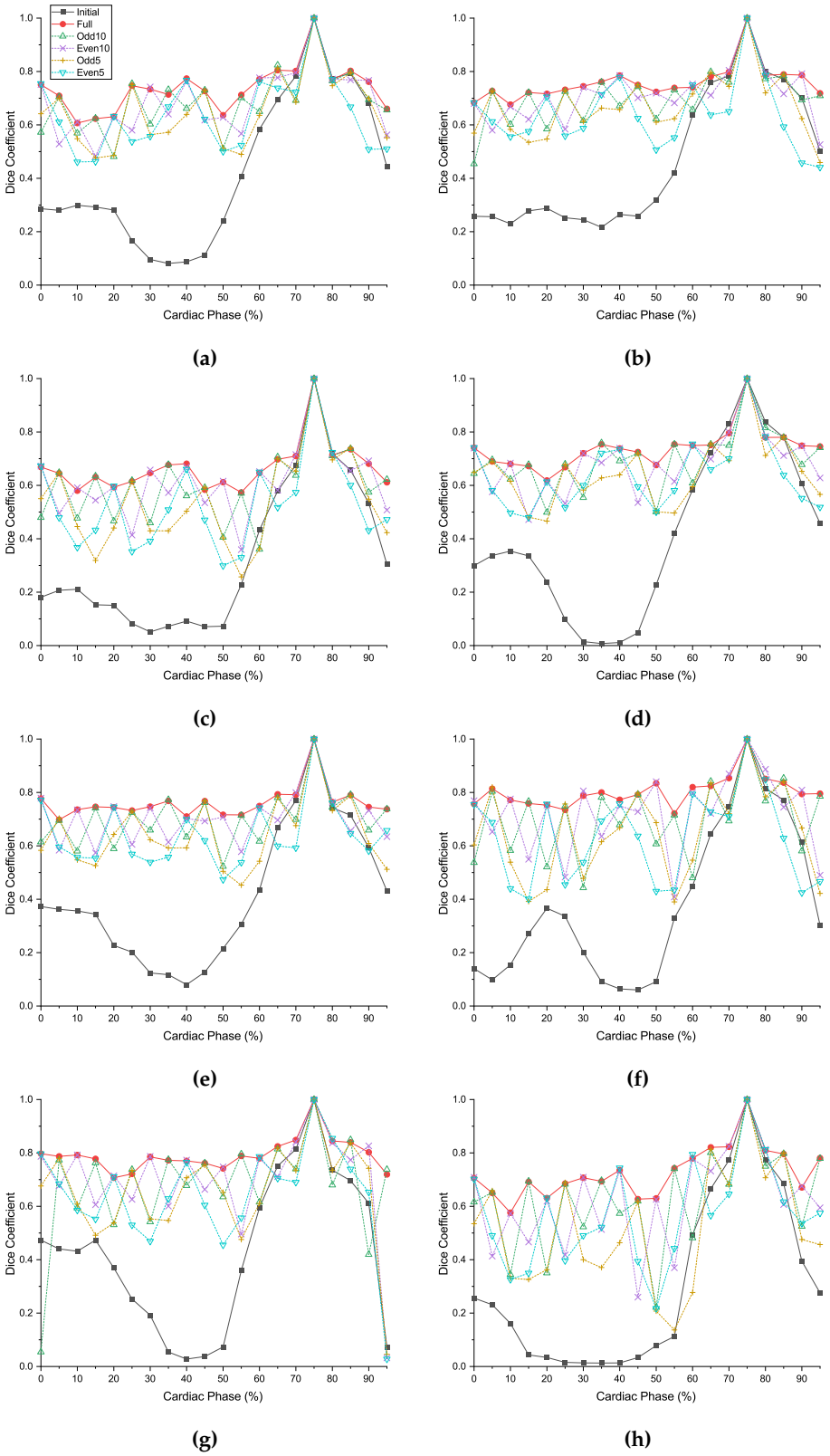

Figure A5. (a)-(h)Dice coefficients between target model to deformed models at the different cardiac phase.

Preprints (www.preprints.org) | NOT PEER-REVIEWED | Posted: 4 September 2020 doi:10.20944/preprints202009.0085.v1

Appendix A.6. Average distances for different phase sampling methods

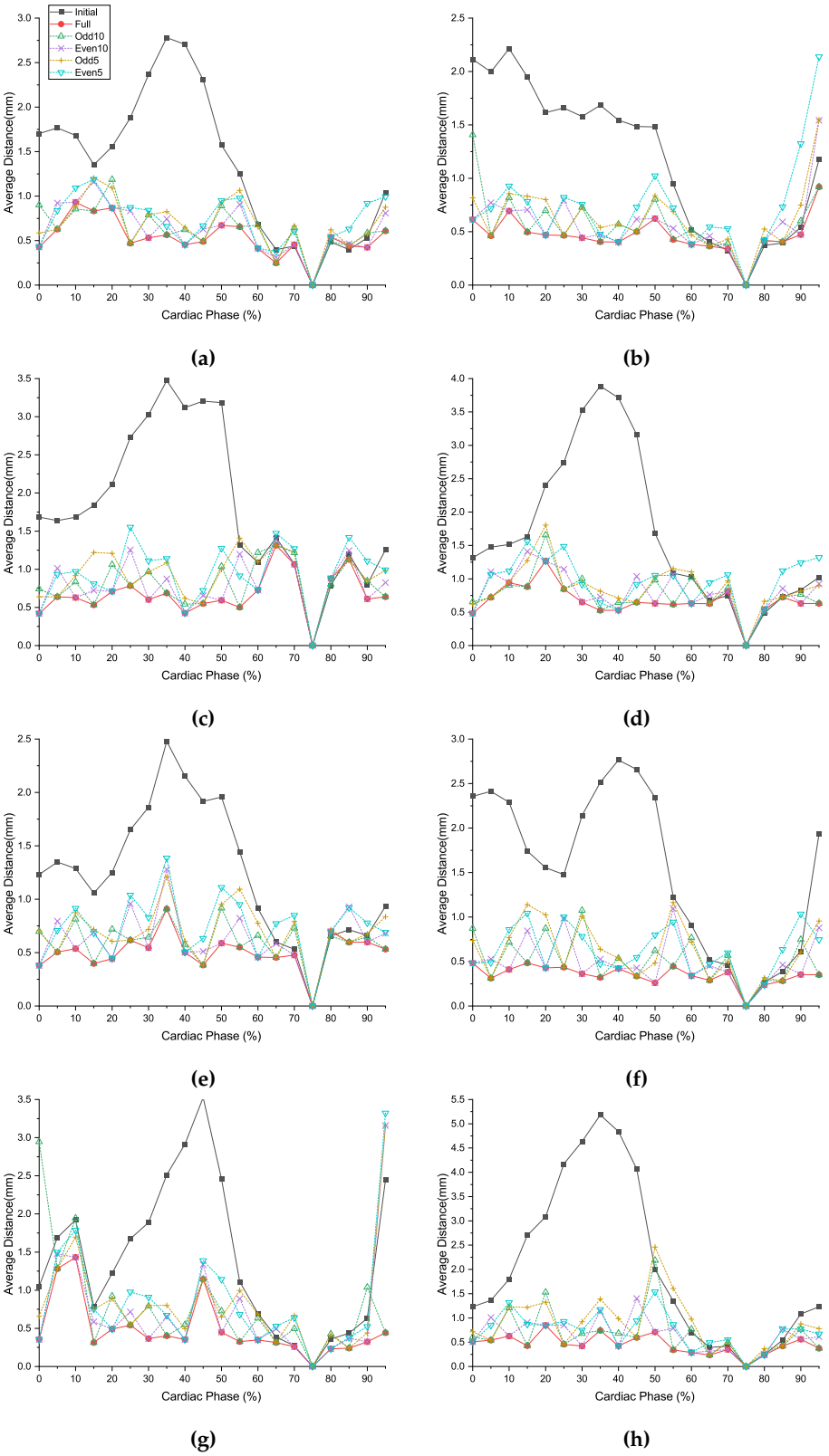

Figure A6. (a)-(h)Average distances between target model to deformed models at the different cardiac phase.

References

1. Virani, S.S.; Alonso, A.; Benjamin, E.J.; Bittencourt, M.S.; Callaway, C.W.; Carson, A.P.; Chamberlain, A.M.; Chang, A.R.; Cheng, S.; Delling, F.N.; others. s1) Heart disease and stroke statistics—2020 update a report from the American Heart Association. *Circulation* **2020**, pp. E139–E596.
2. Hadjiiski, L.; Zhou, C.; Chan, H.P.; Chughtai, A.; Agarwal, P.; Kuriakose, J.; Kazerooni, E.; Wei, J.; Patel, S. Coronary CT angiography (cCTA): automated registration of coronary arterial trees from multiple phases. *Physics in Medicine & Biology* **2014**, *59*, 4661.
3. Zeng, S.; Feng, J.; An, Y.; Lu, B.; Lu, J.; Zhou, J. Towards Accurate and Complete Registration of Coronary Arteries in CTA Images. International Conference on Medical Image Computing and Computer-Assisted Intervention. Springer, 2018, pp. 419–427.
4. Biglarian, M.; Larimi, M.M.; Afrouzi, H.H.; Moshfegh, A.; Toghraie, D.; Javadzadegan, A.; Rostami, S. Computational investigation of stenosis in curvature of coronary artery within both dynamic and static models. *Computer methods and programs in biomedicine* **2020**, *185*, 105170.
5. Wu, X.; von Birgelen, C.; Muramatsu, T.; Li, Y.; Holm, N.R.; Reiber, J.H.; Tu, S. A novel four-dimensional angiographic approach to assess dynamic superficial wall stress of coronary arteries in vivo: initial experience in evaluating vessel sites with subsequent plaque rupture. *EuroIntervention* **2017**, *13*, e1099–e1103.
6. Elattar, M.A.; Vink, L.W.; van Mourik, M.S.; Baan Jr, J.; vanBavel, E.T.; Planken, R.N.; Marquering, H.A. Dynamics of the aortic annulus in 4D CT angiography for transcatheter aortic valve implantation patients. *Plos one* **2017**, *12*, e0184133.
7. Shi, B.; Katsevich, G.; Chiang, B.S.; Katsevich, A.; Zamyatin, A. Image registration for motion estimation in cardiac CT. Medical Imaging 2014: Physics of Medical Imaging. International Society for Optics and Photonics, 2014, Vol. 9033, p. 90332E.
8. Forte, M.N.V.; Valverde, I.; Prabhu, N.; Correia, T.; Narayan, S.A.; Bell, A.; Mathur, S.; Razavi, R.; Hussain, T.; Pushparajah, K.; others. Visualization of coronary arteries in paediatric patients using whole-heart coronary magnetic resonance angiography: comparison of image-navigation and the standard approach for respiratory motion compensation. *Journal of Cardiovascular Magnetic Resonance* **2019**, *21*, 1–9.
9. Coppo, S.; Piccini, D.; Bonanno, G.; Chaptinel, J.; Vincenti, G.; Feliciano, H.; Van Heeswijk, R.B.; Schwitter, J.; Stuber, M. Free-running 4D whole-heart self-navigated golden angle MRI: initial results. *Magnetic resonance in medicine* **2015**, *74*, 1306–1316.
10. Li, S.; Xie, Z.; Xia, Q.; Hao, A.; Qin, H. Hybrid 4D cardiovascular modeling based on patient-specific clinical images for real-time PCI surgery simulation. *Graphical Models* **2019**, *101*, 1–7.
11. Lamash, Y.; Fischer, A.; Carasso, S.; Lessick, J. Strain analysis from 4-D cardiac CT image data. *IEEE Transactions on Biomedical Engineering* **2014**, *62*, 511–521.
12. Gupta, V.; Lantz, J.; Henriksson, L.; Engvall, J.; Karlsson, M.; Persson, A.; Ebbers, T. Automated three-dimensional tracking of the left ventricular myocardium in time-resolved and dose-modulated cardiac CT images using deformable image registration. *Journal of cardiovascular computed tomography* **2018**, *12*, 139–148.
13. Li, Q.; Tong, Y.; Yin, Y.; Cheng, P.; Gong, G. Definition of the margin of major coronary artery bifurcations during radiotherapy with electrocardiograph-gated 4D-CT. *Physica Medica* **2018**, *49*, 90–94.
14. Liu, B.; Bai, X.; Zhou, F. Local motion-compensated method for high-quality 3D coronary artery reconstruction. *Biomedical optics express* **2016**, *7*, 5268–5283.
15. Chen, M.Y.; Shanbhag, S.M.; Arai, A.E. Submillisievert median radiation dose for coronary angiography with a second-generation 320–detector row CT scanner in 107 consecutive patients. *Radiology* **2013**, *267*, 76–85.
16. Besl, P.J.; McKay, N.D. Method for registration of 3-D shapes. Sensor fusion IV: control paradigms and data structures. International Society for Optics and Photonics, 1992, Vol. 1611, pp. 586–606.
17. Sorkine, O.; Alexa, M. As-rigid-as-possible surface modeling. Symposium on Geometry processing, 2007, Vol. 4, pp. 109–116.
18. Davatzikos, C. Spatial transformation and registration of brain images using elastically deformable models. *Computer Vision and Image Understanding* **1997**, *66*, 207–222.

19. Pennec, X.; Stefanescu, R.; Arsigny, V.; Fillard, P.; Ayache, N. Riemannian elasticity: A statistical regularization framework for non-linear registration. International Conference on Medical Image Computing and Computer-Assisted Intervention. Springer, 2005, pp. 943–950.
20. Burger, M.; Modersitzki, J.; Ruthotto, L. A hyperelastic regularization energy for image registration. *SIAM Journal on Scientific Computing* **2013**, *35*, B132–B148.
21. Chiang, M.C.; Leow, A.D.; Klunder, A.D.; Dutton, R.A.; Barysheva, M.; Rose, S.E.; McMahon, K.L.; De Zubicaray, G.I.; Toga, A.W.; Thompson, P.M. Fluid registration of diffusion tensor images using information theory. *IEEE transactions on medical imaging* **2008**, *27*, 442–456.
22. Vercauteren, T.; Pennec, X.; Perchant, A.; Ayache, N. Symmetric log-domain diffeomorphic registration: A demons-based approach. International conference on medical image computing and computer-assisted intervention. Springer, 2008, pp. 754–761.
23. Yeo, B.T.; Vercauteren, T.; Fillard, P.; Peyrat, J.M.; Pennec, X.; Golland, P.; Ayache, N.; Clatz, O. DT-REFinD: Diffusion tensor registration with exact finite-strain differential. *IEEE transactions on medical imaging* **2009**, *28*, 1914–1928.
24. Younes, L.; Qiu, A.; Winslow, R.L.; Miller, M.I. Transport of relational structures in groups of diffeomorphisms. *Journal of mathematical imaging and vision* **2008**, *32*, 41–56.
25. Cootes, T.F.; Taylor, C.J.; Cooper, D.H.; Graham, J. Active shape models-their training and application. *Computer vision and image understanding* **1995**, *61*, 38–59.
26. Glocker, B.; Komodakis, N.; Navab, N.; Tziritas, G.; Paragios, N. Dense registration with deformation priors. International Conference on Information Processing in Medical Imaging. Springer, 2009, pp. 540–551.
27. Baka, N.; Metz, C.; Schultz, C.; Neefjes, L.; van Geuns, R.J.; Lelieveldt, B.P.; Niessen, W.J.; van Walsum, T.; de Bruijne, M. Statistical coronary motion models for 2D+ t/3D registration of X-ray coronary angiography and CTA. *Medical image analysis* **2013**, *17*, 698–709.
28. Yang, X.; Xue, Z.; Liu, X.; Xiong, D. Topology preservation evaluation of compact-support radial basis functions for image registration. *Pattern Recognition Letters* **2011**, *32*, 1162–1177.
29. Donato, G.; Belongie, S. Approximate thin plate spline mappings. European conference on computer vision. Springer, 2002, pp. 21–31.
30. Sederberg, T.W.; Parry, S.R. Free-form deformation of solid geometric models. Proceedings of the 13th annual conference on Computer graphics and interactive techniques, 1986, pp. 151–160.
31. Sdika, M. A fast nonrigid image registration with constraints on the Jacobian using large scale constrained optimization. *IEEE transactions on medical imaging* **2008**, *27*, 271–281.
32. Rueckert, D.; Aljabar, P.; Heckemann, R.A.; Hajnal, J.V.; Hammers, A. Diffeomorphic registration using B-splines. International Conference on Medical Image Computing and Computer-Assisted Intervention. Springer, 2006, pp. 702–709.
33. Chui, H.; Rangarajan, A. A new point matching algorithm for non-rigid registration. *Computer Vision and Image Understanding* **2003**, *89*, 114–141.
34. Chui, H.; Rangarajan, A. A feature registration framework using mixture models. Proceedings IEEE Workshop on Mathematical Methods in Biomedical Image Analysis. MMBIA-2000 (Cat. No. PR00737). IEEE, 2000, pp. 190–197.
35. Jian, B.; Vemuri, B.C. A robust algorithm for point set registration using mixture of Gaussians. Tenth IEEE International Conference on Computer Vision (ICCV'05) Volume 1. IEEE, 2005, Vol. 2, pp. 1246–1251.
36. Myronenko, A.; Song, X.; Carreira-Perpinán, M.A. Non-rigid point set registration: Coherent point drift. Advances in neural information processing systems, 2007, pp. 1009–1016.
37. Myronenko, A.; Song, X. Point set registration: Coherent point drift. *IEEE transactions on pattern analysis and machine intelligence* **2010**, *32*, 2262–2275.
38. Jian, B.; Vemuri, B.C. Robust point set registration using gaussian mixture models. *IEEE transactions on pattern analysis and machine intelligence* **2010**, *33*, 1633–1645.
39. Ma, J.; Qiu, W.; Zhao, J.; Ma, Y.; Yuille, A.L.; Tu, Z. Robust *L_{2}E* estimation of transformation for non-rigid registration. *IEEE Transactions on Signal Processing* **2015**, *63*, 1115–1129.
40. Ma, J.; Zhao, J.; Yuille, A.L. Non-rigid point set registration by preserving global and local structures. *IEEE Transactions on image Processing* **2015**, *25*, 53–64.

41. Yushkevich, P.A.; Piven, J.; Cody Hazlett, H.; Gimpel Smith, R.; Ho, S.; Gee, J.C.; Gerig, G. User-Guided 3D Active Contour Segmentation of Anatomical Structures: Significantly Improved Efficiency and Reliability. *Neuroimage* **2006**, *31*, 1116–1128.
42. Seifarth, H.; Wienbeck, S.; Pusken, M.; Juergens, K.U.; Maintz, D.; Vahlhaus, C.; Heindel, W.; Fischbach, R. Optimal systolic and diastolic reconstruction windows for coronary CT angiography using dual-source CT. *American Journal of Roentgenology* **2007**, *189*, 1317–1323.
43. Press, W.H.; Teukolsky, S.A.; Vetterling, W.T.; Flannery, B.P. *Numerical recipes 3rd edition: The art of scientific computing*; Cambridge university press, 2007.
44. OpenMP Architecture Review Board. OpenMP Application Program Interface Version 3.0, 2008.
45. Pheatt, C. Intel® threading building blocks. *Journal of Computing Sciences in Colleges* **2008**, *23*, 298–298.